Bulletin of the Seismological Society of America, Vol. 107, No. 5, pp. 2416–2426, October 2017, doi: 10.1785/0120160393

# The 2015 $M_w$ 8.3 Illapel, Chile, Earthquake: Direction-Reversed Along-Dip Rupture with Localized Water Reverberation

by Chao An, Han Yue, Jianbao Sun, Lingsen Meng, and Juan Carlos Báez

**Abstract** The kinematic rupture process of the 2015 Illapel, Chile, earthquake is investigated based on a joint inversion of teleseismic, Interferometric Synthetic Aperture Radar, Global Positioning System, and tsunami data, as well as backprojection (BP) techniques. The coseismic slip area is determined to be ~100 × 100 km along strike and along dip, with a peak slip of ~7.0 m located ~80 km to the north-northeast of the epicenter. The total seismic moment is estimated to be $2.5 \times 10^{21}$ N·m ($M_w$ 8.2). The rupture kinematics is featured by unilateral propagation along the strike and reverse rupture along the dip. In our model, the rupture bifurcates to up-dip and down-dip between 20 and 40 s. The downward rupture branch reaches the down-dip border of the rupture area at 30–40 s, reverses its propagation direction, and migrates to the trench between 80 and 100 s. This is also revealed in the BP results in a wide frequency range. The aftershocks on the plate interface are complementary to the coseismic rupture area. Normal-faulting aftershocks are observed in the out-trench area, and its along-strike extent is consistent with that of the near-trench rupture. To determine the source duration of the main event, we compare the teleseismic waveforms of the mainshock and aftershocks at different depths. Coda waves after 100 s are observed in both the mainshock and shallow aftershock waveforms, with similar duration, relative amplitude, and characteristic period (16 s). This is consistent with a theoretical water-reverberation-phase period near the trench. Therefore, it suggests that the coda waves likely originate from water reverberation generated by shallow rupture, instead of from a prolonged source duration.

*Electronic Supplement:* Figures of data fitting in the inversion, animated figure of the rupture process, and table describing the Interferometric Synthetic Aperture Radar (InSAR) data.

## Introduction

The Nazca plate is subducting beneath the South American plate at a rate of 60–70 mm/yr (Schellart *et al.*, 2011) along the Peru–Chile trench (Fig. 1). This convergent tectonic plate boundary has been hosting many megathrust earthquakes, accounting for 18 out of 95 global earthquakes greater than $M_w$ 8.0 (Aron *et al.*, 2013), including the 1960 $M_w$ 9.5 Valdivia event, the largest earthquake in modern history of seismology (Kanamori and Cipar, 1974). The most recent two large-thrust events are the 2014 $M_w$ 8.2 Iquique and the 2015 $M_w$ 8.3 Illapel earthquakes. In central Chile, the megathrust segment near Illapel was identified as a seismic gap that previously ruptured in the 1943 $M_w$ 7.9 earthquake (Beck *et al.*, 1998). On 16 September 2015 22:54:33 UTC, this region was shocked by an $M_w$ 8.3 event near Illapel, Chile. The rupture lasted for about 100 s and generated a 4.5-m-high tsunami wave along the coast of Coquimbo. The Global Centroid Moment Tensor (CMT) solution (Ekström *et al.*, 2012) for this event suggests almost purely double-couple faulting, with strike $\phi = 7°$, dip $\delta = 19°$, rake $\lambda = 109°$, and a scalar moment of $3.23 \times 10^{21}$ N·m ($M_w$ 8.3).

After the 2015 Illapel earthquake, numerous slip models are developed from different observations and inversion techniques. Most of these models derive a unilateral rupture to the north of the epicenter (e.g., Heidarzadeh *et al.*, 2016; Li *et al.*, 2016; Melgar *et al.*, 2016; Ruiz *et al.*, 2016; Tilmann *et al.*, 2016), but some studies resolve significant slip to the south (e.g., U.S. Geological Survey [USGS] results; Lee *et al.*, 2016; Ye *et al.*, 2016). Refer to Ji *et al.* (2002, 2003) and Shao *et al.* (2011) for more technical details of

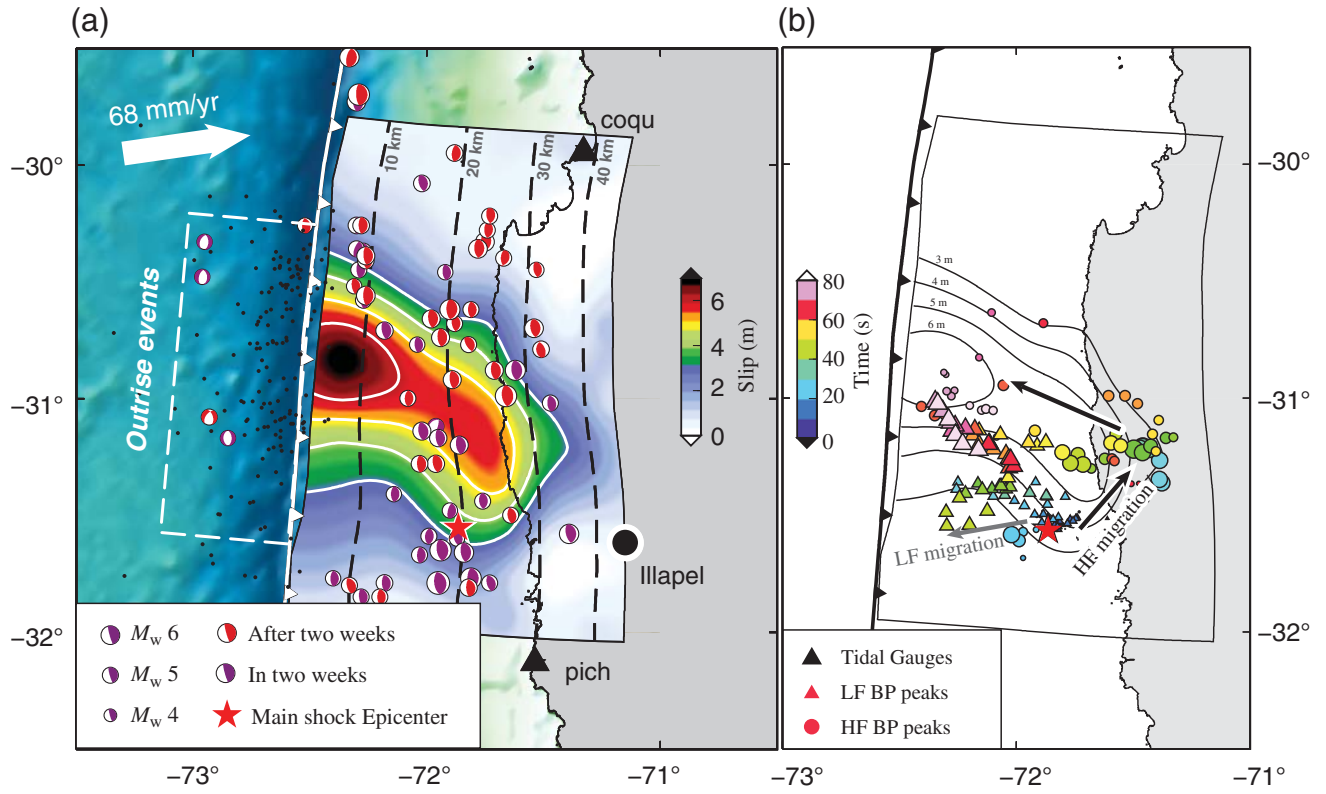


**Figure 1.** (a) The red star marks the Centro Sismológico Nacional, Chile, epicenter (71.864° W, 31.553° S), and the dashed black lines indicate the depth of the slab interface. The coseismic slip pattern is plotted in color-filled contours. Early (within two weeks) and later aftershocks are plotted with red- and purple-filled focal mechanisms, respectively. Epicentral locations of the Preliminary Determined Earthquake catalog are plotted as black dots for outrise aftershocks, with the area of outrise events marked by a white dashed box. The tide-gauge stations are shown in black-filled triangles. (b) The backprojection (BP) results are compared with the coseismic slip patterns. The high-frequency (HF) and low-frequency (LF) BP radiators are plotted as circles and triangles, respectively, with the time denoted by color. The migration direction of HF and LF radiators are indicated with black and gray arrows, respectively.

the USGS results. Additionally, the source duration estimated in most studies is less than 100 s (Heidarzadeh *et al.*, 2016; Li *et al.*, 2016; Melgar *et al.*, 2016; Ye *et al.*, 2016). However, Lee *et al.* (2016) perform a finite-fault inversion using Green's functions (GFs) computed from a 3D spectral-element method and suggest that a very long source duration of ~250 s is necessary to fit the coda waves. Also, existing rupture models show significant variation of the near-trench slip, with either large (>4 m) (Lee *et al.*, 2016; Li *et al.*, 2016; Melgar *et al.*, 2016; Solaro *et al.*, 2016; Ye *et al.*, 2016) or small (<4 m) (Heidarzadeh *et al.*, 2016; Ruiz *et al.*, 2016) amount of slip. In addition to finite-fault inversions, backprojection (BP) studies of this earthquake reveal a depth-dependent radiation behavior (Melgar *et al.*, 2016; Tilmann *et al.*, 2016; Yin *et al.*, 2016). The high-frequency (HF) energy is found to mainly radiate from the down-dip rupture.

To further resolve and test the discrepancies reported in previous models, for example, the lateral extent, peak slip amount, and source duration, we employ a joint inversion of teleseismic body waves, Interferometric Synthetic Aperture Radar (InSAR), Global Positioning System (GPS), and tsunami data to derive the rupture process of the 2015 Illapel earthquake. We also utilize BP and empirical Green's function (EGF) analysis to determine the energy release history in the kinematic rupture process.

## Data and Model Parameterization

The teleseismic dataset consists of 18 *P* and 26 *SH* body waves with epicentral distances between 40° and 95° (Fig. 2a). A reflectivity method (Kikuchi *et al.*, 1993) is used to compute the GFs, which accounts for body-wave interactions in different 1D-layered structures on the source and receiver sides. Instead of assuming uniform water depth, the thickness of the water layer in the source area is interpolated from the ETOPO1 bathymetry database to better calculate the characteristic water-reverberation phases in teleseismic GFs. The water depth at each row of the finite-fault grids is averaged in the along-strike direction and then added to the 1D velocity model at the source side. The 1D velocity structure beneath the water layer is incorporated from the CRUST 1.0 model (Laske *et al.*, 2013), it is also used for computation of the GFs for the InSAR and tsunami observations.

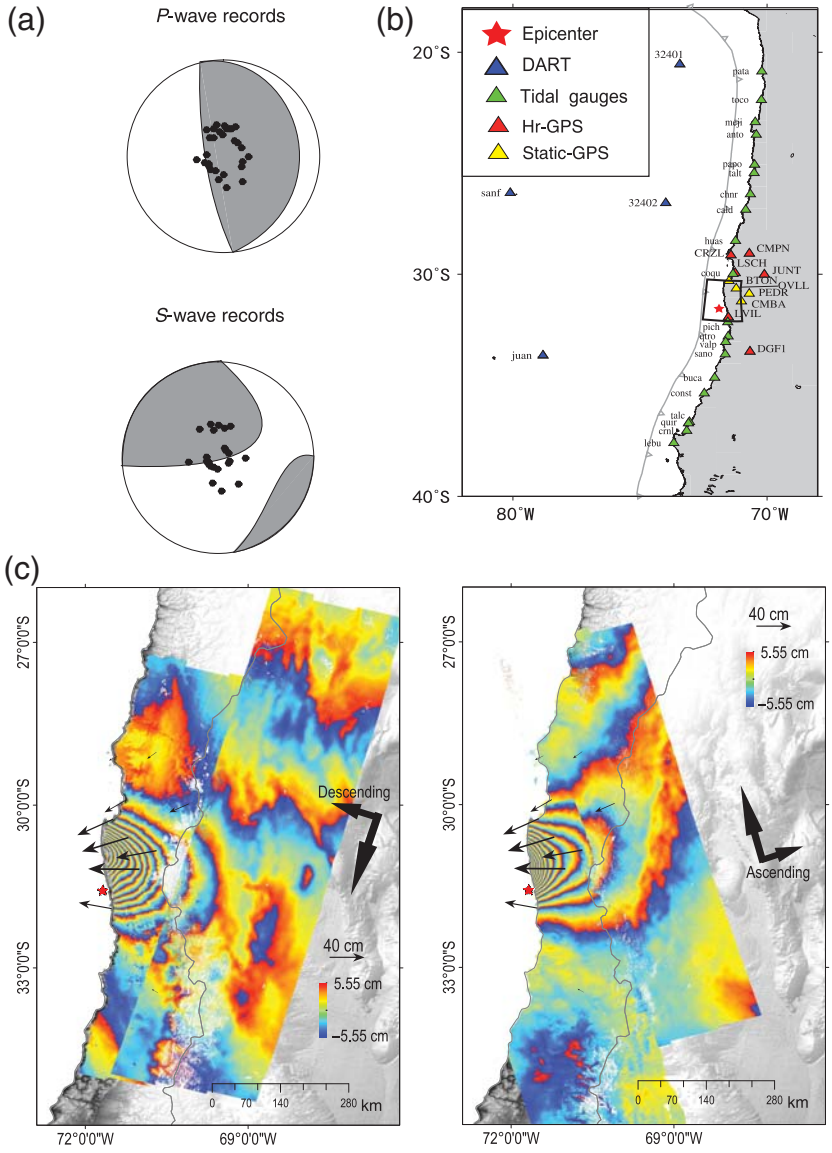


**Figure 2.** (a) The teleseismic *P* and SH records are projected to the focal sphere and masked on the *P* and *SH* radiation patterns, respectively. (b) The 22 tide gauges, 2 Deep-ocean Assessment and Reporting of Tsunamis (DART) stations, 6 high-rate Global Positioning System (Hr-GPS), and 4 static GPS stations are plotted in green-, blue-, red-, and yellow-filled triangles, respectively. Note that the Hr-GPS stations are also used as static GPS stations. The source area is indicated by a black rectangle. (c) The rewrapped Synthetic Aperture Radar interferometry images are plotted for descending and ascending tracks in the left and right panels, respectively. The heading and looking directions are marked for each image.

We utilize four tracks of Sentinel-1A Synthetic Aperture Radar (SAR) data in both ascending and descending passes from the European Space Agency (ESA) for InSAR processing. They are acquired with Interferometric Wide Swath mode, and the data of each date are composed of three subswaths and assembled with a succession of 5–6 slices of SAR data (Ⓔ see Table S1, available in the electronic supplement to this article). We use both the Sentinel Application Platform software provided by ESA and the InSAR scientific computing environment software from the Jet Propulsion Laboratory (JPL)/California Institute of Technology (Caltech) (Rosen *et al.*, 2012) to process the data. The precise orbit data from ESA are applied to improve the InSAR coherence. The Shuttle Radar Topography Mission digital elevation model data (Farr *et al.*, 2007) are used for topographic phase removal, and a global optimization algorithm is adopted for phase unwrapping (Strozzi *et al.*, 2008). We also estimate and remove a linear ramp from the unwrapped data using the static GPS displacements measured near the epicenter (Fig. 2c) or the overlap region with nearby track data (Fig. 2c). Higher-order orbit ramps are inverted later in the joint inversion, so that the mixed deformation and long wavelength trends can be further separated. Using a quad-tree algorithm (Jónsson *et al.*, 2002), the unwrapped InSAR interferograms are decimated to 1361 and 1482 line-of-sight samples in the ascending and descending tracks, respectively. The GFs are computed using the static ground displacements generated from a rectangular dislocation source in the CRUST 1.0 model (Wang *et al.*, 2003).

During the Illapel earthquake, the Global Navigation Satellite Systems (GNSS) data are recorded at 1 Hz (e.g., Chen *et al.*, 2016). The data are processed using the Bernese GPS Software v.5.2 (Dach and Walser, 2015), with precise orbit and earth rotation parameters from the International GNSS Service (IGS) final products (Dow *et al.*, 2009). The processing strategy is carried out in two steps: we first use 3 days of GNSS data from 10 stations at the earthquake region plus 15 selected IGS regional stations to estimate the position before the earthquake (double-difference mode). For the datum definition, we use the minimum constraint approach, applying the no-net-rotation and no-net-translation conditions for the regional IGS stations. At the second step, we select five of the IGS reference stations from the far field, and each other station is processed in a kinematic mode. As a result, we recover the static displacements (coseismic) and the kinematic trajectory. The high-rate GPS (Hr-GPS) data are band-pass filtered between 10 and 200 s and then downsampled at 2 s intervals. The GFs for the Hr-GPS data are computed using a frequency–wavenumber integration algorithm (Zhu and Rivera, 2002), and then band-pass filtered and downsampled using the same parameters as used in processing the data. The GFs for static

GPS data are computed using a similar algorithm as for the InSAR data (Wang *et al.*, 2003).

The tsunami data used in this study are collected from 2 Deep-ocean Assessment and Reporting of Tsunamis (DART) and 22 coastal gauges (Fig. 2b), retrieved from the National Oceanic and Atmospheric Administration and the Intergovernmental Oceanographic Commission, respectively. To calculate the GFs, the parallelized linear version of Cornell Multigrid Coupled Tsunami Model (COMCOT) (Liu *et al.*, 1998; An *et al.*, 2014) is used to simulate the tsunami waves. The bathymetry data used in this study are the GEBCO_2014 (General Bathymetric Chart of the Oceans) data with a resolution of 30 arcsec. The timestep in the simulation is 1.0 s, and the total computational time is 12,000 s. Because the tsunami waves are more accurately simulated at DART stations (because of less wave nonlinearity due to deeper water depth), the weighting for DART records is assigned to be 10 times that for the coastal records based on the number of DART stations and coastal gauges. The contribution of horizontal seafloor deformation is taken into account by considering the seafloor tomography variation (Tanioka and Satake, 1996). The tsunami GFs are shifted in time according to the initial rupture time to account for the finite rupture process of the earthquake.

To determine the along-strike extent of the rupture area, we first parameterize the fault model with coarse grids that cover a relatively large region (400 km along strike and 100 km along dip, Fig. 3a). A joint inversion of all the datasets is performed to identify the principal slip zone (30°–32° S), which is then parameterized with finer girds. In the fine-grid setting, the fault plane consists of $12 \times 7$ subfaults, and the subfault dimension is $\sim 20 \times 20$ km. The fault geometry is adapted to a 3D curved-slab interface obtained from gravity observations (Tassara and Echaurren, 2012). Two rakes of 91° and 121° are used to compute the GFs for each dataset, allowing subevent rakes on subfaults to vary within $106° \pm 15°$ in a nonnegative inversion. The central rake value is taken from the Global CMT focal mechanism. A uniform rupture velocity of 2.8 km/s is adopted to calculate the initial time of each subfault, which is the maximum speed inferred from BP analysis using the USArrays. The subfault source time function is parameterized with 35 triangles with a 2 s rise time, allowing a source duration of 72 s to fully cover the rupture process. Our tests show that, if the rupture velocity is less than 2.8 km/s, the moment rate will be truncated to the head of the source time functions at downdip subfaults (see e.g., 2.0 km/s, Ⓔ Fig. S8). The combination of high rupture velocity and long source duration is selected to ensure a fast-enough rupture front and a long-enough rupture duration to cover the complete rupture process. Based on multiple tests with different weighting combinations, we choose relative weighting of 0.2, 0.1, 0.2, and 1.0 for teleseismic, tsunami, GPS, and InSAR datasets, respectively, after normalizing the data and GFs by the mean of absolute values of observations. Such relative weighting is selected with respect to the residual versus weight trade-off curve of each dataset and the resulting stability (Yue *et al.*, 2016).

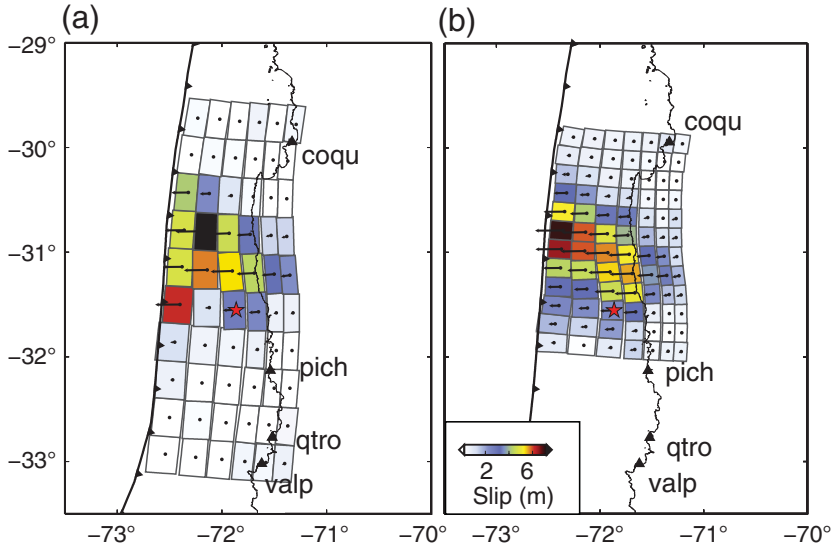


**Figure 3.** (a) The coseismic slip pattern obtained with the coarse grids is plotted in a white–black color scale. The subfault dimension is $\sim 20 \times 40$ km$^2$. (b) The coseismic slip pattern obtained from the fine grids is plotted. The subfault dimension is $\sim 20 \times 20$ km$^2$. In both panels, the epicenter is marked with a red-filled star, and the tide gauges are denoted by black triangles.

The coseismic rupture process of the 2015 $M_w$ 8.3 Illapel earthquake is also imaged by the BP method (Ishii *et al.*, 2005; Krüger and Ohrnberger, 2005; Lange *et al.*, 2016; Melgar *et al.*, 2016; Yin *et al.*, 2016). Here we adopt the Multitaper-MUSIC array processing technique, which resolves more closely spaced sources and is less sensitive to aliasing, yielding a sharper image of the rupture process than the standard beamforming approach (Meng *et al.*, 2011). We also apply a reference window strategy, which eliminates so-called swimming artifacts, a systematic apparent drift of the HF energy toward the station arrays (Meng *et al.*, 2012). The BP analysis is typically performed on coherent seismograms recorded at teleseismic distances. Here, we use the seismograms recorded by the U.S. seismic network (US), composed of 522 broadband stations evenly distributed across the continental United States with epicentral distances between 60° and 95°. We band-pass filter the seismograms between 2 and 0.5 s, the highest band with relatively high waveform coherency. We align the initial *P*-wave arrivals of the filtered waveforms with a multichannel cross-correlation technique. The first arrival is assumed to come from the Centro Sismológico Nacional hypocenter location (71.864° W, 31.553° S, Fig. 1). The location of the later HF sources

is determined based on the differential travel time relative to the hypocenter. A layered ak135 velocity model (Kennett *et al.*, 1995) is adopted to compute the travel time as a function of epicentral distance. Because differential travel time is not sensitive to relatively small source depth changes along the shallow-dipping plate interface, we backproject the waveforms onto a horizontal fault plane at a depth of 15 km.

## Results and Discussion

### Coseismic Slip Distribution

Our preferred model is chosen to match the aftershock locations and the slip deficit (~7 m) since the last large earthquake. It is shown in Figure 3a,b for coarse- and fine-grid settings, respectively. The coarse-grid setting allows for a large rupture extent in the along-strike direction, but the coseismic rupture is constrained within a compact area between 30.5° and 31.5° S. Minor slip is resolved to the south of the epicenter. The coseismic rupture area has been investigated by numerous studies using inversion or tsunami-wave forward-modeling techniques, and some of them find significant slip (> 2 m) to the south of the epicenter (USGS results; Lange *et al.*, 2016; Lee *et al.*, 2016; Ye *et al.*, 2016). It is noticeable that none of those models include tsunami data in the analysis. In contrast, all the rupture models that incorporate tsunami data resolve minor slip (< 2 m) to the south of the epicenter (e.g., Heidarzadeh *et al.*, 2016; Lay *et al.*, 2016; Li *et al.*, 2016; Melgar *et al.*, 2016). Thus, tide-gauge records provide strong constraints to the along-strike extent of the rupture zone. As demonstrated by Lay *et al.* (2016), large slip to the south of 31.5° S would result in earlier predictions of tsunami waves than recorded at the southern tide gauges.

Our model in the fine-grid setting indicates that the down-dip limitation of coseismic rupture extends to ~40 km in depth, in a compact area around 31.2° S. The down-dip slip distributions are mainly constrained by the on-land geodetic observations. Source models lacking constraints from on-land geodesy generally predict the down-dip rupture widely distributed in a large area (e.g., Heidarzadeh *et al.*, 2016; Okuwaki *et al.*, 2016). Melgar *et al.* (2016) include InSAR and GPS data in their joint inversion work and resolve a compact down-dip rupture pattern with slip up to 10 m near the coastline. Such large slip produces relatively large InSAR residuals (~0.4 m) in the coastal area. Our model presents maximum down-dip slip of ~5 m, and the standard deviation of InSAR residual of each interferogram is less than 0.05 m. Such discrepancy may be introduced by the relative weighting of different datasets. The peak slip is determined to be ~7 m located close to the trench and ~80 km along strike from the epicenter. The near-trench slip extends ~100 km between 30.5° and 31.5° S, which is consistent with the rupture pattern revealed by Li *et al.* (2016). Melgar *et al.* (2016) estimate a longer along-strike extent of ~200 km, which leads to earlier predictions of tsunami-wave arrivals at northern tide gauges (Station HUAS in fig. S2b in their supplementary information). The amount of near-trench slip also varies in different studies from ~4 (e.g., Heidarzadeh *et al.*, 2016) to ~10 m (e.g., Li *et al.*, 2016; Melgar *et al.*, 2016). In previous source inversion studies, the near-trench slip can be well constrained by offshore tsunami data, especially when the tsunami observations are recorded in the trench normal direction (An *et al.*, 2014; Lay *et al.*, 2014; Yue, Lay, Rivera, An, *et al.*, 2014). In this study, all the four offshore tsunami stations are oblique from the trench normal direction (JUAN, SANF, 32402, 32401, Fig. 2b), thus the constraints to the near-trench rupture are not as ideal as in the 2014 Iquique case. In our analysis, inversion with only tsunami and InSAR data produces a near-trench slip of ~4 m. The amount of slip increases without degrading the tsunami waveform fits when teleseismic and GPS data are added. Thus, the significant slip (> 4 m) near the trench (< 40 km from trench) is compatible with all datasets.

For several well-studied big earthquakes, the aftershocks are complimentary to the coseismic slip zone (e.g., Yue, Lay, Rivera, An, *et al.*, 2014). This phenomenon is also observed in the Illapel earthquake aftershock sequence (Lange *et al.*, 2016; Melgar *et al.*, 2016). As shown in Figure 1a, most of the aftershocks occurred around the 3-m coseismic-slip contour, indicating that they were triggered by shear-stress concentration near the rupture tips. Very few aftershocks were found in the area, with large slip (> 6 m) where complete stress drop could have occurred. Additionally, a cluster of outrise normal-faulting events are identified between 30° and 31.5° S, which might be caused by the dilatational stress change introduced by the near-trench thrusting (Xu *et al.*, 2016; Yue, Lay, Rivera, Bai, *et al.*, 2014).

### Rupture Kinematics

The kinematic rupture process is illustrated in Figure 4, in which the moment release and BP results within every 10 s are plotted in each panel. The BP analysis utilizes teleseismic recordings of USArray at HF (0.5–2.0 Hz), low frequency (LF, 0.05–0.5 Hz), and very low frequency (VLF, 0.01–0.1 Hz) to beamform energy bursts at different frequency bands. The LF and VLF BP results are of lower resolution than the HF results and are less effective in resolving closely spaced sources. Here, we focus on interpreting the locations of peak BP radiator locations, which can be regarded as the centroids of the energy release in their respective frequency range. In the first 20 s, a low moment release is resolved within a small area near the hypocenter, corresponding to a relatively quiescent period in the first 20 s of teleseismic recordings. A similar quiescent period is also found in several other large megathrust events (e.g., the 2014 Iquique and 2011 Tohoku earthquakes). During 20–40 s, VLF and HF radiators bifurcate to the up-dip and down-dip, respectively, which is consistent with the along-dip expansion of the kinematic slip model. Similar depth-dependent BP migration for this event has also been reported by Melgar *et al.* (2016) and

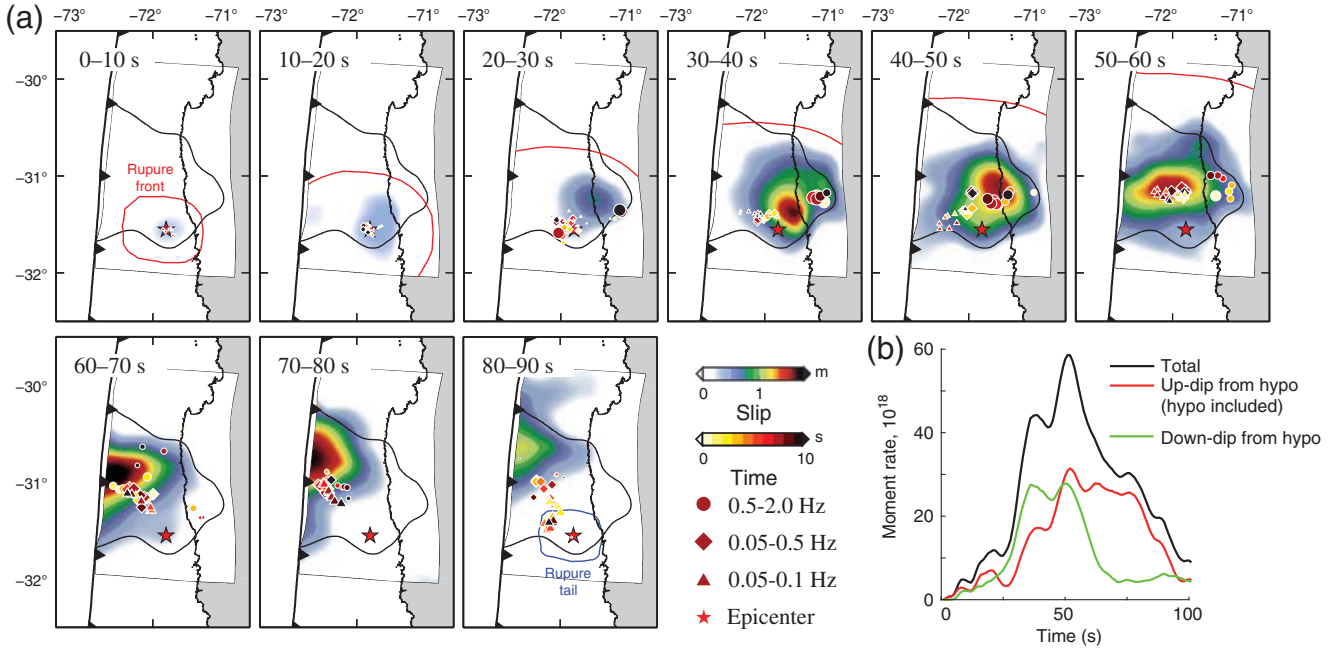


**Figure 4.** The kinematic rupture process is plotted in (a) with a 10-s time interval. BP radiators at HF, LF, and very low-frequency (VLF) bands are plotted as circles, triangles, and diamonds, respectively. The symbols are color-coded from white to red by time, with reference time being the starting time of each interval, to illustrate the energy radiation migration. The rupture front and tail are plotted with red and blue curves. The moment rate functions are given in (b).

Yin *et al.* (2016). Between 40 and 50 s, the main rupture area migrates from down-dip to the central depth, which is consistent with the migration of HF radiators. At the same time, the LF radiators migrate along strike to the same area. Between 50 and 60 s, the main slip area migrates up-dip, consistent with the LF and VLF radiators. At the same time, there is still significant HF energy radiated from the down-dip rupture. Between 60 and 90 s, the main rupture continues to migrate to the trench, and the HF, LF, and VLF BP radiators show the same trend. At this period, the LF and VLF radiators match the rupture area in the along-dip direction, albeit presenting ~20 km offset from the peak slip area in the along-strike direction. Moment-rate functions are plotted in Figure 4b, which clearly demonstrate that the moment release is dominated by the down-dip rupture (deeper than the hypocenter) before 60 s and by up-dip rupture after 60 s.

The finite-fault model and BP analysis consistently reveal a complicated rupture process. The rupture to the down-dip migrates back to the central rupture area and then moves to the trench. A similar zigzag along-dip rupture is also reported by Okuwaki *et al.* (2016) from HF BP analysis. Melgar *et al.* (2016) adopt a short subfault slip duration (20 s) and demonstrate that a pulse-like rupture tracks the BP migration. In this work, we allow a much longer time window (72 s) without forcing a pulse-like rupture; however, our result still presents significant consistency between the BP radiators and kinematic-source models. Animated comparison is provided in Ⓔ Figure S7 for detailed comparison in shorter time intervals. In general, down-dip rupture (> 20 km in depth) shows more correlation with HF radiators, up-dip rupture (< 10 km in depth) is more correlated with LF and VLF radiators, and rupture at intermediate depths (10–20 km) radiates energy at all frequency bands. This depth-dependent rupture behavior has been widely reported for many megathrust events (Lay *et al.*, 2012).

## Moment Release after 100 s

The majority of the published kinematic rupture models parameterize the source duration within 120 s, so rupture is not allowed to happen beyond this time in the models (e.g., Lay *et al.*, 2016; Melgar *et al.*, 2016; Ye *et al.*, 2016). Lee *et al.* (2016) adopt a 3D velocity model to compute seismic GFs and invert teleseismic body and surface waves for a kinematic slip model. Their results indicate a two-stage rupture process, with the first stage accounting for a moment release before 100 s and a second after 100 s. The second stage has an equivalent magnitude of $M_w$ 8.08 and produces significantly improved waveform fitting to seismic recordings after 100 s. Lee *et al.* (2016) also demonstrate that the significant codas between 100 and 180 s are not shown in the waveforms of two local aftershocks, that is, EGFs. Using a deconvolution method, Lee *et al.* (2016) resolve a 240-s-long source time function with a similar shape as that resolved by the kinematic rupture model. Lay *et al.* (2016) suggest that the coda waves of teleseismic recordings may originate from water-reverberation phases. In this study, we use water depth on top of the shallowest grids to match the bathymetry near the trench (~6 km) and reproduce similar fits of teleseismic

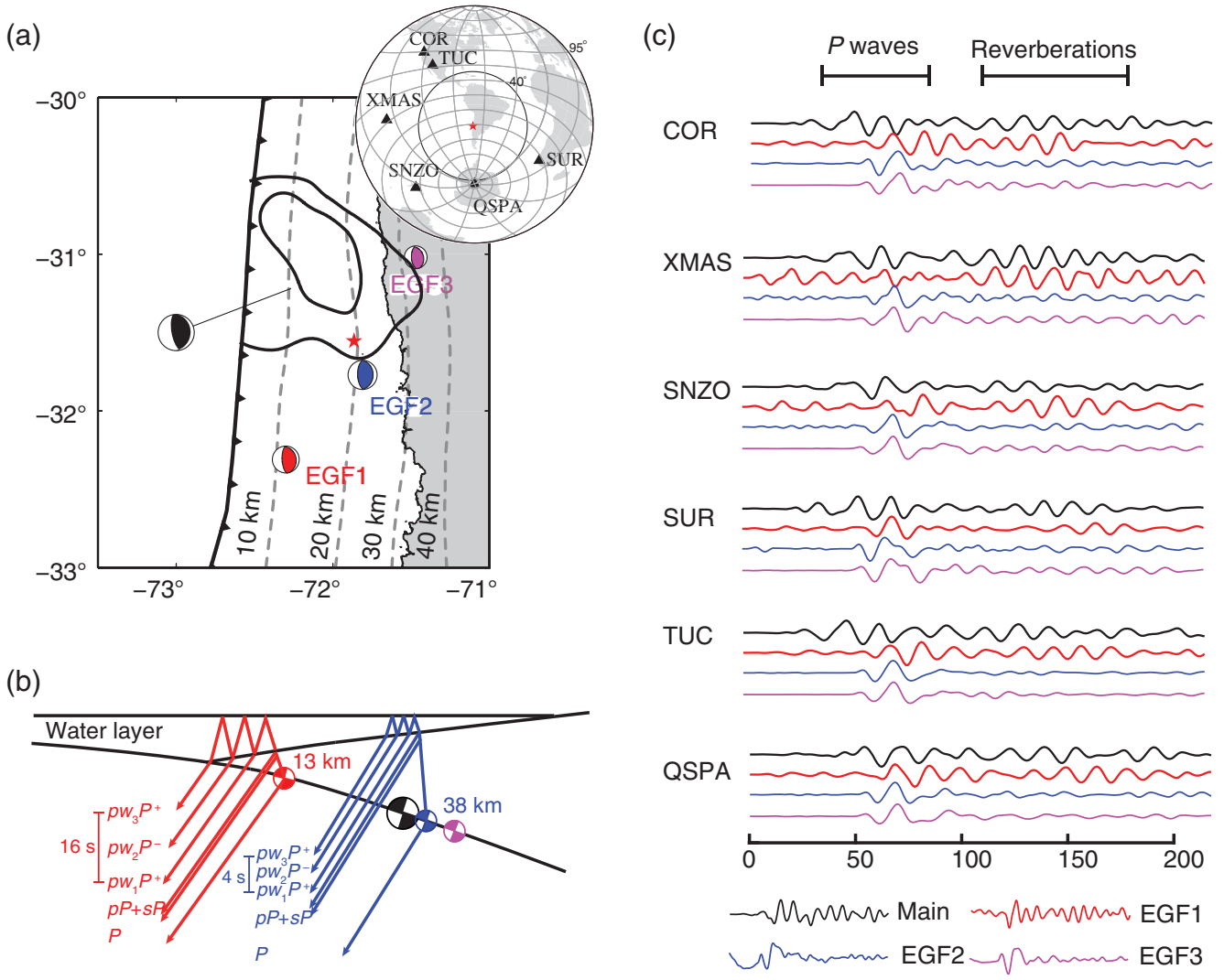


**Figure 5.** (a) The mainshock slip distribution is plotted in black contours, with the epicentral location marked by a red-filled star. Empirical Green's functions (EGFs) are shown with red-, blue-, and magenta-filled focal mechanisms. The same color is used to plot ray paths and seismic waveforms in (b) and (c). (b) The depth cross section is plotted to show the *pwP* paths. For EGF1 (red) at shallow depth (13 km) with a thick water layer (6 km), the characteristic period of *pwP* phase is ∼16 s; for EGF2 (blue) at deeper depth (38 km) with a thin water layer (1.5 km), the characteristic period of *pwP* phase is ∼4 s. (c) The mainshock waveforms are plotted in black, and the waveforms for EGF events are plotted in red, blue, and magenta, respectively. Water-reverberation phases are identified in the mainshock waveforms and EGF1, whereas they are not observed in deep EGFs.

*P*-wave codas as given by Lay *et al.* (2016). Thus, a prolonged source is not required to fit the observed teleseismic coda waves.

EGFs from two aftershocks are used by Lee *et al.* (2016) for comparison with the main event. The depths of the two events are around 30 km, which is close to the main event hypocentral depth. However, kinematic rupture models obtained by Lee *et al.* (2016) and our study both resolve significant slip near the trench. Thus, the EGFs used by Lee *et al.* (2016) are ineffective in presenting the characteristic waveform of the whole rupture area. From the Illapel aftershock sequence, we select one shallow event, located close (<40 km) to the trench, with hypocentral depth of 13.5 km (Global CMT solution), to compare with the main event Figure 5 (parameters of the three EGFs are provided in Ⓔ Table S2). A band-pass filter of 0.01–0.1 Hz is applied to all waveforms to remove HF noises for clear comparison with coda waves. A triangle-shaped source time function, with 6 s rise time, is convolved with the EGFs to produce similar pulse width as the mainshock. The STF of 6 s is chosen, based on empirical tests, to produce comparable source-related pulse width at the time segment of source waves for the mainshock and the EGFs. The EGFs are shifted back by ∼45 s to align with the major peaks of the main event. It is clearly demonstrated in Figure 5 that both the main event waveforms and shallow EGF present significant coda waves between 100 and 180 s, with a similar reverberation period at 16 s. The two deeper EGFs present no

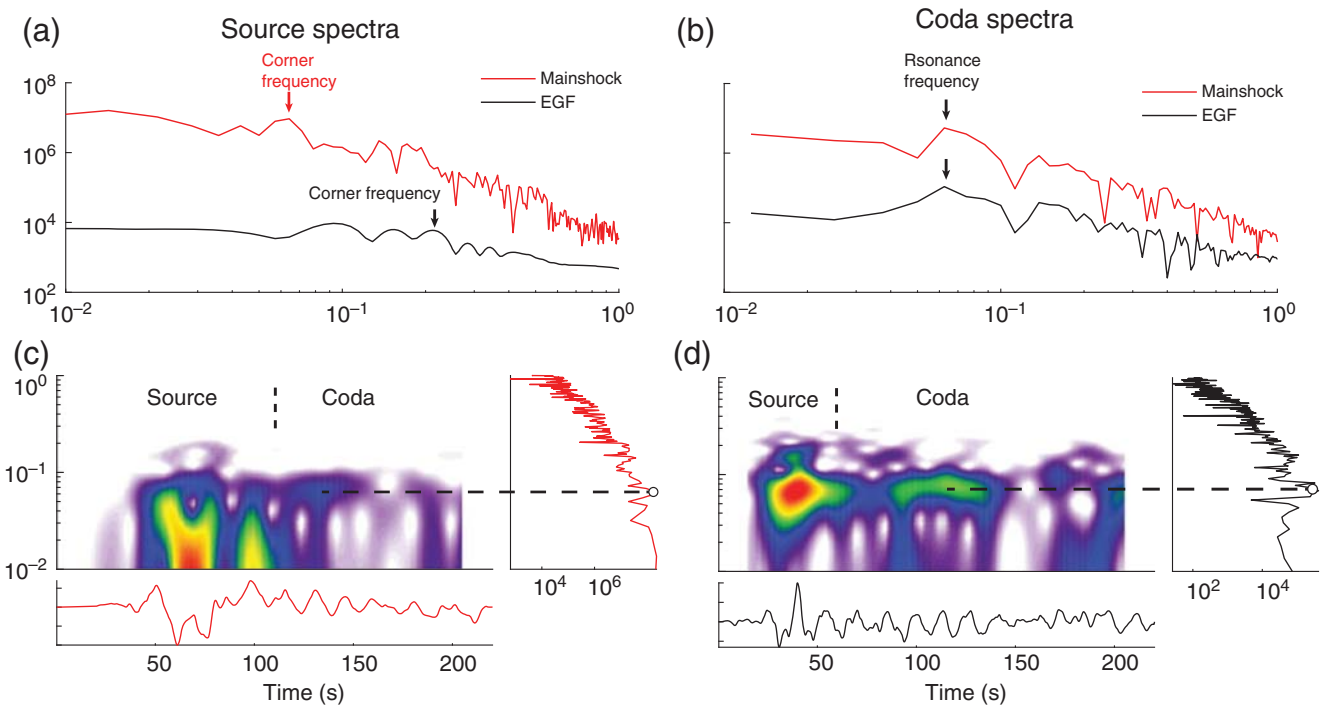


**Figure 6.** (a,b) Spectra of the teleseismic displacement waveforms at Station TUC for the source and coda segments, respectively. In each subplot, the mainshock and EGF-related spectra are plotted in red and black, respectively. The time window of the source and coda segments is different for the main and EGF waveforms, and it is indicated in (c,d). (c,d) Spectrogram of the mainshock and EGF waveforms, respectively. In each subplot, the spectrogram is imaged in the center, with the waveform and total spectrum plotted at the bottom and on the right panel, respectively. A characteristic period of ~16 s is identified between 100 and 150 s, corresponding to a peak period of ~16 s observed in the spectrum of the complete records. This characteristic period is inferred to be associated with the water-reverberation phases.

significant coda at this time period, as also demonstrated by Lee *et al.* (2016). Thus, the coda waves likely originate from the structural-related phases excited by the near-trench rupture. Compressional waves (*P* waves) reflected at the water surface reverse their polarity, so the characteristic period of water-reverberation phases (*pwP*) equals two times the *P*-wave round traveling time in the water layer ($pw_1P$ and $pw_3P$, or $pw_2P$ and $pw_4P$, etc.). Assuming the near-trench water depth is ~6 km, and the *P* wavespeed is 1.5 km/s, the theoretical *pwP* period of 16 s is consistent with the observed *P*-wave coda in both the main event and the shallow aftershock. The water-reverberation phases of the two deeper EGFs have a dominant period of 3 s and decay fast after the *pP* and *sP* arrival, which explains why the coda waves are not observed in deep EGFs. Comparison of waveforms from the mainshock and shallow and deep EGFs at more stations are shown in Ⓔ Figure S9.

We calculate the spectrograms of both the mainshock and the shallow EGF event from the displacement waveforms at Station TUC and show the spectrograms and spectra of the complete records in Figure 6c,d. At the segment of coda waves, that is, 100–150 s for the mainshock and 40–110 s for the EGF, both spectrograms present peak amplitudes at around 16 s, which is the period of water reverberation. In Figure 6a,b, it is observed that the coda spectra have consistent peaks at around 16 s for both the mainshock and the shallow EGF, whereas the source spectra are flat at LF and drop by a power law beyond the corner frequency. This indicates that the coda waves are not directly from the earthquake-rupture processes.

To further elaborate the idea, we also compare the teleseismic *P*-coda waves of two megathrust earthquakes that take place along the Chilean coast, the 2010 Maule and 2014 Iquique earthquakes. Previous studies show that the Maule earthquake has significant rupture (> 10 m) near the trench (e.g., Yue, Lay, Rivera, An, *et al.*, 2014), in comparison with minor near-trench rupture during the Iquique earthquake (e.g., An *et al.*, 2014; Lay *et al.*, 2014). In Ⓔ Figure S10, it is observed that the Maule event is associated with prolonged coda waves after 100 s, whereas the Iquique earthquake has relatively clean waveforms at this time segment. This is consistent with the different efficiency of exciting water-reverberation phases from shallow and deep ruptures, as analyzed for the Illapel mainshock and EGFs. On the other hand, the *P*-wave codas in the Maule event show more complexity than in the Illapel event, which could be caused by the bilateral rupture near the trench. Nevertheless, the first-order consistency between the Maule,

Iquique, and Illapel earthquakes indicates that such localized water-reverberation phases can be commonly excited by near-trench ruptures of megathrust events.

Localized water-reverberation phases are also found for outrise strike-slip events, for example, the 2012 $M_w$ 7.2 Indian Ocean earthquake and its EGF event (Yue *et al.*, 2017). The water-reverberation phases are observed in the teleseismic *P*-coda waves in the seaward direction from the trench. Yue *et al.* (2017) conclude that a sharp bathymetry gradient near the trench can modify the *Pw* and *Sw* waves to form standing waves near the trench, with characteristic frequency consistent with the water-reverberation period. Similar water-reverberation phases are also found for previous megathrust events, for example, the 1995 $M_w$ 8.1 Chile and 1994 $M_w$ 8.3 Kurile events (Ihmlé and Madariaga, 1996). The water-reverberation phases of thrust earthquakes, as in the 2010 Maule and 2015 Illapel earthquakes, may be produced by a similar mechanism, that is, a near-trench rupture in the landward direction from the trench.

As demonstrated by Wiens (1989) and Okamoto and Takenaka (2009), the 2D velocity structure and surface geometry influence *pwP* phase significantly, so a 1D velocity model is inefficient to predict water-reverberation phases accurately. Lee *et al.* (2016) use 3D seismic-wave simulations, but the water layer is approximated by a stress boundary condition instead of solving the wave equations in real water. Thus, their synthetics cannot produce the water-reverberation phases accurately. Our analysis using realistic water layer depth explains the characteristic frequency of *pwP* phase reasonably well. Thus, our results present a simple yet reasonable explanation of the coda waves, and moment release after 100 s is not necessary to produce the coda waves.

### Different Modeling and Inversion Techniques

Our preferred ruptured model produces reasonable data fits to all used datasets. Teleseismic and InSAR data are fitted with 74% and 99.92% variance reduction, respectively, which are typical fitting levels for each dataset. At the inverted time segments, tsunami datasets are fitted with 88% of variance reduction. Detailed data fits are plotted in Ⓔ Figures S1–S6 for teleseismic, truncated tsunami, complete tsunami, InSAR, Hr-GPS, and static GPS fits, respectively. (Ⓔ Fig. S6 only shows the six GPS stations near the source.). The source model reliability strongly relies on the accuracy of GF calculations. Lee *et al.* (2016) employ advanced 3D-modeling techniques and obtain a rupture model with improved resolution over 1D teleseismic synthetic-based inversion results (USGS results; Ye *et al.*, 2016). However, lacking constraints from other datasets lead to poor reproduction of tidal-gauge waveforms. Li *et al.* (2016) adopt the tsunami simulation package NEOWAVE to take into account the kinematic excitation of tsunami waves and wave nonlinearity, which provides more accurate simulations at tidal gauges in shallow water. The tsunami-modeling package used in this study (COMCOT) solves linear shallow-water-wave equations, so it is computationally more efficient than NEOWAVE. To reduce the modeling uncertainties at some near-field stations (e.g., PITCH, QTRO, COQU, HAUS), we only adopt the initial ramp of the tsunami recordings (less than a quarter of the wavelength) to avoid matching the full waveform but still keep the constraints of arrival time.

Joint inversion utilizes information from different datasets, in which modeling errors from different datasets are unlikely to produce coherent artifacts. Melgar *et al.* (2016) jointly invert regional seismic, geodetic, and tsunamic data. As one of the first batch of joint models, their model is more reliable in comparison with other models based on inversions of a single dataset (e.g., Ye *et al.*, 2016). The main rupture pattern of Melgar *et al.* (2016) is in agreement with our study, whereas discrepancies also exist in rupture details, for example, lateral extent of the near-trench rupture, slip amount in the down-dip area, and the kinematic rupture process. We infer that these discrepancies can be caused by different choice of model parameters and data preparation, for example, model parameterization, tsunami-wave truncation, the reference velocity model, and relative weighting between datasets. Thus, those parameters are important in joint inversions to resolve rupture details.

## Conclusions

We conducted a joint inversion of teleseismic, InSAR, GPS, and tsunami data to investigate the rupture process of the 2015 $M_w$ 8.3 Illapel earthquake. Several key findings are listed as follows.

1. Our model reveals unilateral and bilateral rupture modes along the strike and dip, respectively. The along-strike rupture extends ~100 km, with no significant slip resolved to the south of the epicenter. The along-dip extent of the principal slip zone covers from the trench to ~40 km in depth.
2. The kinematic rupture process shows high consistency with beamformed teleseismic energy at different frequency bands. Ruptures at shallow, intermediate, and deep depths are associated with VLF, complete frequency, and HF radiators, respectively.
3. Comparison of the coda waves with the EGF waveforms from a shallow event indicates that the coda waves can be originated from water-reverberation phases excited by the shallow rupture. This indicates that the main rupture is not necessarily longer than 100 s.

## Data and Resources

The Global Centroid Moment Tensor (CMT) solution was accessed from http://www.globalcmt.org/CMTsearch.html (last accessed October 2016). The ETOPO1 topography data were retrieved from http://www.ngdc.noaa.gov/docucomp/page?xml=NOAA/NESDIS/NGDC/MGG/DEM/iso/xml/316.xml&view=getDataView&header=none (last accessed October 2016). The Incorporated Research Institu-

tions for Seismology (IRIS) Data Management Center (DMC) was used to access the seismic data from Global Seismic Network and Federation of Digital Seismic Network stations (http://ds.iris.edu/wilber3/find_event, last accessed October 2016). The Synthetic Aperture Radar (SAR) data were acquired by the Sentinel-1A satellite of the European Space Agency (ESA, https://qc.sentinel1.eo.esa.int) and downloaded through Sentinel's Scientific Data Hub (https://scihub.esa.int/dhus/, last accessed October 2016). The tsunami data were downloaded from the National Oceanic and Atmospheric Administration's (NOAA's) website for Deep-ocean Assessment and Reporting of Tsunamis (DART) stations (http://www.ndbc.noaa.gov/dart.shtml, last accessed October 2016) and from the Intergovernmental Oceanographic Commission (IOC) website from coastal gauges (http://www.ioc-sealevelmonitoring.org, last accessed October 2016). The U.S. Geological Survey (USGS) results were taken from the USGS website (http://earthquake.usgs.gov/earthquakes/eventpage/us20003k7a#finite-fault, last accessed September 2016).

## Acknowledgments

This work made use of Generic Mapping Tool (GMT) and Seismic Analysis Code (SAC) software. The freely available software Sentinel Application Platform (SNAP) from the European Space Agency (ESA) was used for Interferometric Synthetic Aperture Radar (InSAR) processing. The simulation of tsunami waves was carried out on the supercomputer Stampede. This work is supported by the National Science Foundation of China (Numbers 41374040 and 41090294); the Hellman Fellowship; a University of California, Los Angeles (UCLA) Faculty Research Grant; the National Aeronautics and Space Administration (NASA) Award NAS7-03001; and the JPL Award 1468977. We thank Thorne Lay, Hiroo Kanamori, Mark Simons, and Lingling Ye for suggestions. We also thank three anonymous reviewers and Associate Editor Diego Melgar for their valuable comments to improve the article. Thanks are also extended to G. Hayes for sharing their finite-fault inversion results on the U.S. Geological Survey (USGS) website.

## References

An, C., I. Sepúlveda, and P. L.-F. Liu (2014). Tsunami source and its validation of the 2014 Iquique, Chile, earthquake, *Geophys. Res. Lett.* **41,** no. 11, 3988–3994.

Aron, F., R. W. Allmendinger, J. Cembrano, G. González, and G. Yáñez (2013). Permanent fore-arc extension and seismic segmentation: Insights from the 2010 Maule earthquake, Chile, *J. Geophys. Res.* **118,** no. 2, 724–739.

Beck, S., S. Barrientos, E. Kausel, and M. Reyes (1998). Source characteristics of historic earthquakes along the central Chile subduction zone, *J. S. Am. Earth Sci.* **11,** no. 2, 115–129.

Chen, K., M. Ge, A. Babeyko, X. Li, F. Diao, and R. Tu (2016). Retrieving real-time co-seismic displacements using GPS/GLONASS: A preliminary report from the September 2015 $M_w$ 8.3 Illapel earthquake in Chile, *Geophys. J. Int.* **206,** no. 2, 941–953.

Dach, R., and P. Walser (2015). Bernese GNSS Software Version 5.2, *User Manual*, Astronomical Institute, University of Bern, Bern, Switzerland.

Dow, J. M., R. Neilan, and C. Rizos (2009). The international GNSS service in a changing landscape of global navigation satellite systems, *J. Geodes.* **83,** nos. 3/4, 191–198.

Ekström, G., M. Nettles, and A. M. Dziewoński (2012). The global CMT project 2004–2010: Centroid-moment tensors for 13,017 earthquakes, *Phys. Earth Planet. In.* **200,** 1–9.

Farr, T. G., P. A. Rosen, E. Caro, R. Crippen, R. Duren, S. Hensley, M. Kobrick, M. Paller, E. Rodriguez, L. Roth, *et al.* (2007). The shuttle radar topography mission, *Rev. Geophys.* **45,** no. 2, doi: 10.1029/2005RG000183.

Heidarzadeh, M., S. Murotani, K. Satake, T. Ishibe, and A. R. Gusman (2016). Source model of the 16 September 2015 Illapel, Chile, $M_w$ 8.4 earthquake based on teleseismic and tsunami data, *Geophys. Res. Lett.* **43,** no. 2, 643–650.

Ihmlé, P. F., and R. Madariaga (1996). Monochromatic body waves excited by great subduction zone earthquakes, *Geophys. Res. Lett.* **23,** no. 21, 2999–3002.

Ishii, M., P. M. Shearer, H. Houston, and J. E. Vidale (2005). Extent, duration and speed of the 2004 Sumatra–Andaman earthquake imaged by the Hi-Net array, *Nature* **435,** no. 7044, 933–936.

Ji, C., D. V. Helmberger, D. J. Wald, and K. F. Ma (2003). Slip history and dynamic implications of the 1999 Chi-Chi, Taiwan, earthquake, *J. Geophys. Res.* **108,** no. B9, doi: 10.1029/2002JB001764.

Ji, C., D. J. Wald, and D. V. Helmberger (2002). Source description of the 1999 Hector Mine, California earthquake, part I: Wavelet domain inversion theory and resolution analysis, *Bull. Seismol. Soc. Am.* **92,** no. 4, 1192–1207.

Jónsson, S., H. Zebker, P. Segall, and F. Amelung (2002). Fault slip distribution of the 1999 $M_w$ 7.1 Hector Mine, California, earthquake, estimated from satellite radar and GPS measurements, *Bull. Seismol. Soc. Am.* **92,** no. 4, 1377–1389.

Kanamori, H., and J. J. Cipar (1974). Focal process of the great Chilean earthquake May 22, 1960, *Phys. Earth Planet. In.* **9,** no. 2, 128–136.

Kennett, B., E. Engdahl, and R. Buland (1995). Constraints on seismic velocities in the Earth from traveltimes, *Geophys. J. Int.* **122,** no. 1, 108–124.

Kikuchi, M., H. Kanamori, and K. Satake (1993). Source complexity of the 1988 Armenian earthquake: Evidence for a slow after-slip event, *J. Geophys. Res.* **98,** no. B9, 15,797–15,808.

Krüger, F., and M. Ohrnberger (2005). Tracking the rupture of the $M_w = 9.3$ Sumatra earthquake over 1,150 km at teleseismic distance, *Nature* **435,** no. 7044, 937–939.

Lange, D., J. Geersen, S. Barrientos, M. Moreno, I. Grevemeyer, E. Contreras-Reyes, and H. Kopp (2016). Aftershock seismicity and tectonic setting of the 16 September 2015 $M_w$ 8.3 Illapel earthquake, central Chile, *Geophys. J. Int.* **207,** no. 2, 1424–1430.

Laske, G., G. Masters, Z. Ma, and M. Pasyanos (2013). Update on CRUST1.0—A 1-degree global model of Earth's crust, *Geophys. Res. Abstr.* **15,** 2658.

Lay, T., H. Kanamori, C. J. Ammon, K. D. Koper, A. R. Hutko, L. Ye, H. Yue, and T. M. Rushing (2012). Depth-varying rupture properties of subduction zone megathrust faults, *J. Geophys. Res.* **117,** no. B04311, doi: 10.1029/2011JB009133.

Lay, T., L. Li, and K. F. Cheung (2016). Modeling tsunami observations to evaluate a proposed late tsunami earthquake stage for the 16 September 2015 Illapel, Chile, $M_w$ 8.3 earthquake, *Geophys. Res. Lett.* **43,** no. 15, 7902–7912.

Lay, T., H. Yue, E. E. Brodsky, and C. An (2014). The 1 April 2014 Iquique, Chile, $M_w$ 8.1 earthquake rupture sequence, *Geophys. Res. Lett.* **41,** no. 11, 3818–3825.

Lee, S.-J., T.-Y. Yeh, T.-C. Lin, Y.-Y. Lin, T.-R. A. Song, and B.-S. Huang (2016). Two-stage composite megathrust rupture of the 2015 $M_w$ 8.4 Illapel, Chile, earthquake identified by spectral-element inversion of teleseismic waves, *Geophys. Res. Lett.* **43,** no. 10, 4979–4985.

Li, L., T. Lay, K. F. Cheung, and L. Ye (2016). Joint modeling of teleseismic and tsunami wave observations to constrain the 16 September 2015 Illapel, Chile, $M_w$ 8.3 earthquake rupture process, *Geophys. Res. Lett.* **43,** no. 9, 4303–4312.

Liu, P., S. Woo, and Y. Cho (1998). Computer programs for tsunami propagation and inundation, *Technical Report*, Cornell University, Ithaca, New York.

Melgar, D., W. Fan, S. Riquelme, J. Geng, C. Liang, M. Fuentes, G. Vargas, R. M. Allen, P. M. Shearer, and E. J. Fielding (2016). Slip segmentation and slow rupture to the trench during the 2015, $M_w$ 8.3 Illapel, Chile earthquake, *Geophys. Res. Lett.* **43,** no. 3, 961–966.

Meng, L., J. Ampuero, Y. Luo, W. Wu, and S. Ni (2012). Mitigating artifacts in back-projection source imaging with implications for frequency-dependent properties of the Tohoku-Oki earthquake, *Earth Planets Space* **64,** no. 12, 1101–1109.

Meng, L., A. Inbal, and J. Ampuero (2011). A window into the complexity of the dynamic rupture of the 2011 $M_w$ 9 Tohoku-Oki earthquake, *Geophys. Res. Lett.* **38,** L00G07, doi: 10.1029/2011GL048118.

Okamoto, T., and H. Takenaka (2009). Waveform inversion for slip distribution of the 2006 Java tsunami earthquake by using 2.5 D finite-difference Green's function, *Earth, Planets Space* **61,** no. 5, e17–e20.

Okuwaki, R., Y. Yagi, R. Aránguiz, J. González, and G. González (2016). Rupture process during the 2015 Illapel, Chile earthquake: Zigzag-along-dip rupture episodes, *Pure Appl. Geophys.* **173,** no. 4, 1011–1020.

Rosen, P. A., E. Gurrola, G. F. Sacco, and H. Zebker (2012). The InSAR scientific computing environment, *Proc. of the 9th European Conf. on Synthetic Aperture Radar*, VDE, Nuremberg, Germany, 23–26 April, 730–733.

Ruiz, S., E. Klein, F. del Campo, E. Rivera, P. Poli, M. Metois, V. Christophe, J. C. Baez, G. Vargas, F. Leyton, *et al.* (2016). The seismic sequence of the 16 September 2015 $M_w$ 8.3 Illapel, Chile, earthquake, *Seismol. Res. Lett.* **87,** no. 4, 1–11, doi: 10.1785/0220150281.

Schellart, W., D. Stegman, R. Farrington, and L. Moresi (2011). Influence of lateral slab edge distance on plate velocity, trench velocity, and subduction partitioning, *J. Geophys. Res.* **116,** no. B10, doi: 10.1029/2011JB008535.

Shao, G. F., X. Y. Li, C. Ji, and T. Maeda (2011). Focal mechanism and slip history of the 2011 $M_w$ 9.1 off the Pacific coast of Tohoku earthquake, constrained with teleseismic body and surface waves, *Earth Planets Space* **63,** no. 7, 559–564.

Solaro, G., V. De Novellis, R. Castaldo, C. De Luca, R. Lanari, M. Manunta, and F. Casu (2016). Coseismic fault model of $M_w$ 8.3 2015 Illapel earthquake (Chile) retrieved from multi-orbit Sentinel1-A DInSAR measurements, *Remote Sens.* **8,** no. 4, 323.

Strozzi, T., A. Kouraev, A. Wiesmann, U. Wegmüller, A. Sharov, and C. Werner (2008). Estimation of Arctic glacier motion with satellite L-band SAR data, *Remote Sens. Environ.* **112,** no. 3, 636–645.

Tanioka, Y., and K. Satake (1996). Tsunami generation by horizontal displacement of ocean bottom, *Geophys. Res. Lett.* **23,** no. 8, 861–864.

Tassara, A., and A. Echaurren (2012). Anatomy of the Andean subduction zone: Three-dimensional density model upgraded and compared against global-scale models, *Geophys. J. Int.* **189,** no. 1, 161–168.

Tilmann, F., Y. Zhang, M. Moreno, J. Saul, F. Eckelmann, M. Palo, Z. Deng, A. Babeyko, K. Chen, J. Baez, *et al.* (2016). The 2015 Illapel earthquake, central Chile: A type case for a characteristic earthquake?, *Geophys. Res. Lett.* **43,** no. 2, 574–583.

Wang, R., F. L. Martin, and F. Roth (2003). Computation of deformation induced by earthquakes in a multi-layered elastic crust—FORTRAN programs EDGRN/EDCMP, *Comput. Geosci.* **29,** no. 2, 195–207.

Wiens, D. A. (1989). Bathymetric effects on body waveforms from shallow subduction zone earthquakes and application to seismic processes in the Kurile trench, *J. Geophys. Res.* **94,** no. B3, 2955–2972.

Xu, S., E. Fukuyama, H. Yue, and J.-P. Ampuero (2016). Simple crack models explain deformation induced by subduction zone megathrust earthquakes, *Bull. Seismol. Soc. Am.* **106,** no. 5, 2275–2289.

Ye, L., T. Lay, H. Kanamori, and K. D. Koper (2016). Rapidly estimated seismic source parameters for the 16 September 2015 Illapel, Chile $M_w$ 8.3 earthquake, *Pure Appl. Geophys.* **173,** no. 2, 321–332.

Yin, J., H. Yang, H. Yao, and H. Weng (2016). Coseismic radiation and stress drop during the 2015 $M_w$ 8.3 Illapel, Chile megathrust earthquake, *Geophys. Res. Lett.* **43,** no. 4, 1520–1528.

Yue, H., J. C. Castellanos, C. Yu, L. Meng, and Z. Zhan (2017). Localized water reverberation phases and its impact on back-projection images, *Geophys. Res. Lett.* **44,** doi: 10.1002/2017GL073254.

Yue, H., T. Lay, L. Rivera, C. An, C. Vigny, X. Tong, and J. C. Báez Soto (2014). Localized fault slip to the trench in the 2010 Maule, Chile $M_w = 8.8$ earthquake from joint inversion of high-rate GPS, teleseismic body waves, InSAR, campaign GPS, and tsunami observations, *J. Geophys. Res.* **119,** no. 10, 7786–7804.

Yue, H., T. Lay, L. Rivera, Y. Bai, Y. Yamazaki, K. F. Cheung, E. M. Hill, K. Sieh, W. Kongko, and A. Muhari (2014). Rupture process of the 2010 $M_w$ 7.8 Mentawai tsunami earthquake from joint inversion of near-field hr-GPS and teleseismic body wave recordings constrained by tsunami observations, *J. Geophys. Res.* **119,** no. 7, 5574–5593.

Yue, H., M. Simons, Z. Duputel, J. Jiang, E. Fielding, C. Liang, S. Owen, A. Moore, B. Riel, J. P. Ampuero, *et al.* (2016). Depth varying rupture properties during the 2015 $M_w$ 7.8 Gorkha (Nepal) earthquake, *Tectonophysics* doi: 10.1016/j.tecto.2016.07.005 (in press).

Zhu, L., and L. A. Rivera (2002). A note on the dynamic and static displacements from a point source in multilayered media, *Geophys. J. Int.* **148,** no. 3, 619–627.

School of Naval Architecture, Ocean and Civil Engineering
Shanghai Jiao Tong University
Shanghai 200240, China
(C.A.)

School of Earth and Space Sciences
Peking University
Beijing 100871, China
(H.Y.)

State Key Laboratory of Earthquake Dynamics
Institute of Geology, China Earthquake Administration
Beijing 100029, China
sunjianbao@ies.ac.cn
(J.S.)

Earth, Planetary, and Space Sciences
University of California, Los Angeles
Los Angeles, California 90095
(L.M.)

Centro Sismologico Nacional
Universidad de Chile
Santiago, Chile
(J.C.B.)

Manuscript received 30 December 2016;
Published Online 25 September 2017